Understanding the Conversion Mechanism and Performance of Monodisperse FeF$_2$ Nanocrystal Cathodes

Albert W. Xiao[a], Hyeon Jeong Lee[a], Isaac Capone[a], Alex Robertson[a], Tae-Ung Wi[b],
Jack Fawdon[a], Samuel Wheeler[a], Hyun-Wook Lee[b], Nicole Grobert[a,c], Mauro Pasta[a,*]

a. Department of Materials, University of Oxford
Parks Road, Oxford OX1 3PH, UK
b. School of Energy and Chemical Engineering,
Ulsan National Institute of Science and Technology (UNIST), Ulsan 44919
c. Williams Advanced Engineering, Grove, Oxfordshire, OX12 0DQ, UK
* Correspondence: mauro.pasta@materials.ox.ac.uk, albert.xiao@materials.ox.ac.uk

The application of transition metal fluorides as energy dense cathode materials for lithium ion batteries has been hindered by inadequate understanding of their electrochemical capabilities/limitations. Here, we present an ideal system for mechanistic study through the colloidal synthesis of single crystalline, monodisperse iron(II) fluoride nanorods. Near theoretical capacity (570 mA h g^{-1}) and extraordinary cycling stability (>90% capacity retention after 50 cycles at C/20) is achieved solely through the use of an ionic liquid electrolyte (1 m LiFSI/Pyr$_{1,3}$FSI), which forms a stable solid electrolyte interphase and prevents the fusing of particles. This stability extends over 200 cycles at much higher rates (C/2) and temperatures (50°C). High-resolution analytical transmission electron microscopy reveals intricate morphological features, lattice orientation relationships, and oxidation state changes that comprehensively describe the conversion mechanism. Phase evolution, diffusion kinetics and cell failure are critically influenced by surface specific reactions. The reversibility of the conversion reaction is governed by topotactic cation diffusion through an invariant lattice of fluoride anions and the nucleation of metallic particles on semi-coherent interfaces. This new understanding is used to showcase the inherently high discharge rate capability of FeF$_2$.

Lithium-ion batteries (LIBs) are the industry standard for electrical energy storage. However, higher energy densities are required to match the ever-increasing performance of consumer electronics and power up next-generation electric flights.[1] Current intercalation based electrodes – which store lithium at a fraction of interstitial sites within a stable host structure – are fundamentally limited in their charge storage capacity.[2] Anodes based on the plating/stripping of Li metal or the alloying of Li with Si promise gravimetric capacities nearly ten times greater than that of conventional graphite anodes and are expected to predominate next generation LIBs.[3] However, to effectively utilize these anodes, higher capacity cathodes must also be achieved.

Transition metal fluorides are unique conversion based cathode materials, which react with lithium to form a metallic phase embedded in a lithium fluoride matrix.[4-7] This conversion reaction involves multiple electrons per metal center, resulting in capacities three to five times greater than conventional cathode materials.[4,5,8,9] The higher electrode potentials that enables the use of metal fluorides as cathodes results from highly ionic metal-fluorine bonding.[10] Unfortunately, this same ionic nature also results in low ionic and electronic conductivities.[7,11-13] Foundational electrochemical studies on iron fluorides calculated short diffusion distances (7.6 nm at C/20) and emphasized the need for small particle sizes (<20 nm) to achieve a complete conversion reaction.[7,14] However, in situ microscopy studies on FeF$_2$ have shown discharge over much larger areas at rates estimated between 5-20C.[15,16] Clearly a better understanding of the mechanism is required to determine what limitations are inherent to the material and how they can be mitigated by rational cell design.

Iron(II) fluoride (FeF$_2$) has been widely employed as a model system for mechanistic study.[14,15,18-20] However, the conversion reaction involves the formation of miniscule grains of reaction products and a number of possible intermediate phases.[14,20,21] Definitive conclusions about the conversion mechanism have been hindered by a lack of morphological information and the low spatial resolution of most characterization techniques. Typically, high-resolution transmission electron microscopy (HRTEM) offers little information due to the difficulty of isolating single crystals from a bat-
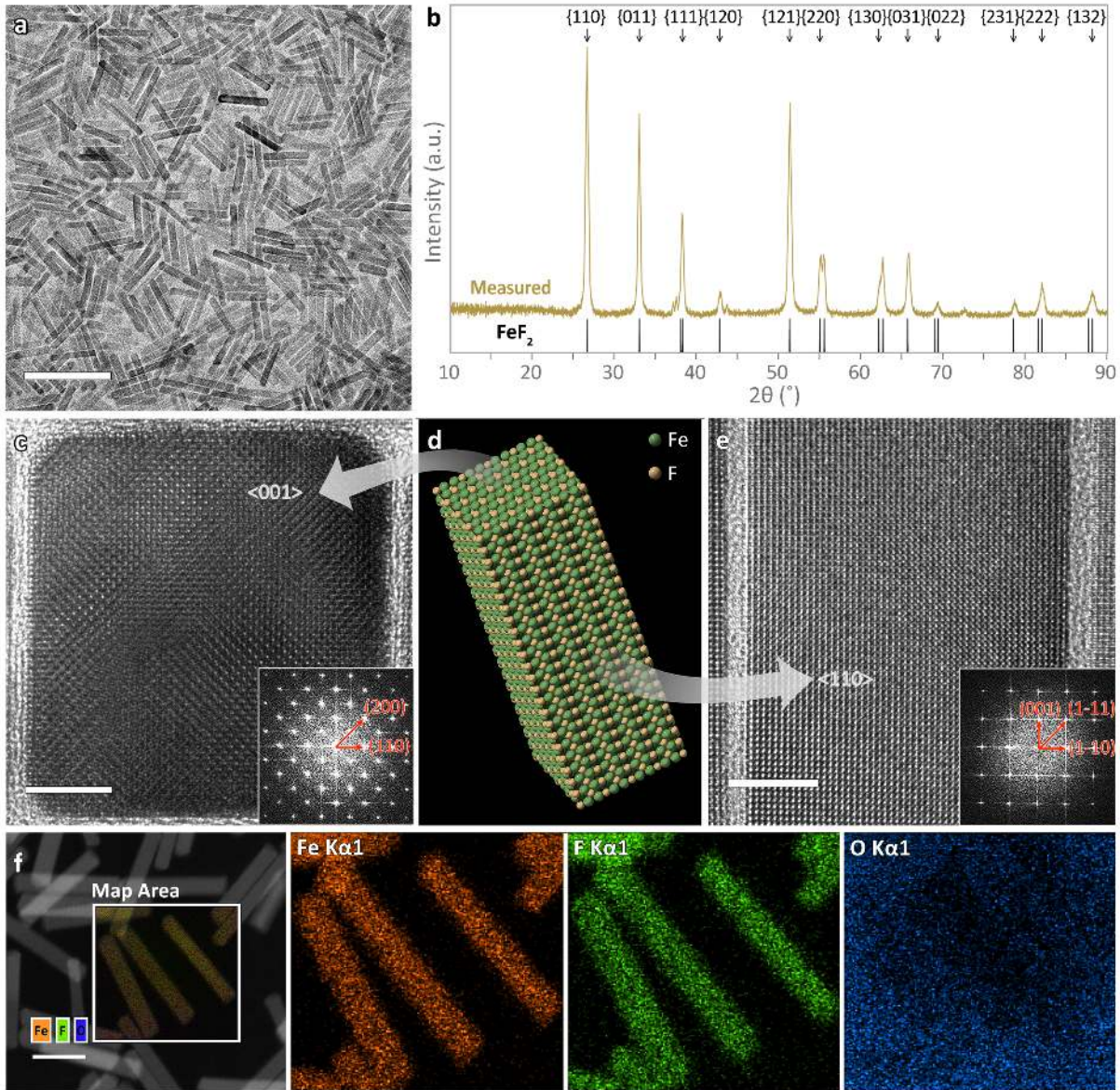
Figure 1: Nanorod Structure and Composition. a, TEM image of as-synthesized FeF_2 nanorods demonstrating an extremely uniform morphology with widths and lengths of $\sim$20 nm and $\sim$100 nm respectively. **b**, Powder XRD pattern of as-synthesized FeF_2 nanorod samples showing phase-pure iron fluoride. Lattice constants indicate no oxygen substitution in the lattice. **c**, HRTEM image of a single FeF_2 nanorod viewed from the end, along the $\langle 0\,0\,1 \rangle$ zone axis. The image shows sharp facets on the $\{1\,1\,0\}$ surfaces and an approximately square cross section; this is expected based on the Wulff theorem and the low surface free energy of the $\{1\,1\,0\}$ planes. The inset reproduces the corresponding FFT, which shows the single and highly crystalline nature of the nanorods; the 4-fold rotational symmetry confirms orientation of the lattice with the $[0\,0\,1]$ along the long axis of the nanorod. **d**, Space-filling model of a single nanorod derived from the standard CIF file of FeF_2, showing the relative orientation of the $\{0\,0\,1\}$ and $\{1\,1\,0\}$ surfaces and overall lattice orientation. Grey arrows demonstrate how a 2D projection of the nanorod along the $\langle 0\,0\,1 \rangle$ and $\langle 1\,1\,0 \rangle$ directions results in the observed TEM images B and D respectively. **e**, HRTEM image of a single FeF_2 nanorod viewed from the side, along the $\langle 1\,1\,0 \rangle$ zone axis. The FFT shown in the inset affirms the lattice orientation derived from B; $\{0\,0\,1\}$ reflections are present as a result of multiple diffraction.[17] FFTs in B and D are set to the same scale. **f**, EDX map of as-synthesized FeF_2 nanorods, which shows strong Fe and F signals and excludes the presence of oxyfluoride. Scale bars, 200 nm (**a**), 5 nm (**c**), 5nm (**e**), 50 nm (**f**).

tery and the impossibility of correlating structure and morphology between disparate particles. However, HRTEM combined with electron energy loss spectroscopy (EELS) is an ideal characterization technique in a system where all particles of the active material are single crystalline and share the same size, morphology, lattice orientation, and exposed facets. Such monodispersity and size/shape

control can be achieved using colloidal synthesis methods.[22,23]

Herein, we present a new one-pot, single-step, high yield method for the colloidal synthesis of FeF$_2$ nanorods from a single source precursor. The resulting 20 nm wide nanorods are single crystalline, monodisperse and faceted so that they naturally fall on a high symmetry zone axis (Figure 1). This system provides well-defined, highly detailed reference frame throughout the conversion reaction and enables the extrapolation of results from individual particles to the entire electrode. Investigation from this unparalleled vantage point redefines the understanding of the conversion reaction. We establish the presence of surface-specific reaction mechanisms and delineate their role in controlling morphology and phase evolution, integrating the computational work of Ma and Garofalini.[11,12] Large-scale lithium diffusion is observed prior to nucleation of metallic iron, and complex phase equilibria involving intermediate phases are revealed, providing long-awaited experimental verification of theoretical predictions.[16,21] We expand on the recent report from Karki *et al.*, defining conversion as a topotactic transformation between fluoride phases.[15] An unprecedented view of the reconversion (delithiation) reaction uncovers considerable chemical and structural symmetry in the reaction pathways. Furthermore, we provide a new rationale for the reversibility of the conversion reaction, based on interfacial coherence and the persistence of the fluoride lattice. Remarkably, this reversibility is manifest in the reformation of pseudo-single crystalline nanorods after the distinctly polycrystalline discharge/charge process.

To enable these mechanistic findings and decisively associate them with the general reversibility of the FeF$_2$ system, we demonstrate the cycling of our material with a capacity of 570 mA h g^{-1} (theoretical: 571 mA h g^{-1}) for over 50 cycles with less than 10% capacity fade using a simple approach. Huang *et al.* showed that electrolyte selection could greatly affect the performance of FeF$_2$ electrodes.[24] In this work, 1 molal lithium bis(fluorosulfonylimide) (LiFSI) dissolved in the N-methyl-N-propyl pyrrolidinium FSI (Pyr$_{1,3}$FSI) ionic liquid is presented as a superior electrolyte for the cycling of transition metal fluorides. The ionic liquid electrolyte precludes major failure mechanisms, preserves the nanorod morphology during cycling, and obviates the use of "strongly coupled" carbon frameworks.[25–29] This electrolyte enables the study of the innate capabilities of FeF$_2$ and the use of simple slurry cast cathodes with superior active material loading (70 wt.%).

FeF$_2$ Nanorods for Mechanistic Evaluation

The colloidal synthesis of FeF$_2$ nanorods is described in the Methods section. The slow rate of the Fe(CF$_3$COO$^-$)$_2$(CF$_3$COOH) precursor decomposition prevents repeated nucleation events, promoting uniform growth. The resultant nanorods are monodisperse (Figure 1A) to the point of spontaneously packing into superlattices, when dried as a powder (Supplementary Figure 1). Surfactants are essential to stabilizing high surface area particles and preventing agglomeration and the consequent growth of irregular morphologies.[22,23] Fourier transformed infrared spectroscopy (FTIR) shows that oleic acid (OLAC) is present as the only capping agent after washing (Supplementary Figure 2). The reduction potential of aliphatic carboxylic acid groups are below 1.0 V vs. Li$^+$/Li respectively.[30] Therefore, oleic acid should not exhibit detrimental redox reactions in the potential window used for galvanostatic cycling.

The tetragonal symmetry of the FeF$_2$ crystal system is reflected in the nanorod morphology. The nanorods exhibit facets dominated by the {1 1 0} planes on the sides and bounded by a curved surface tangent to the {0 0 1} planes on the end (Figure 1D). Faceting causes the rods to naturally fall on their side in the ⟨1 1 0⟩ zone axis orientation (Figure 1E), which is used as a common reference frame to image the conversion reaction. The ⟨0 0 1⟩ zone can be seen from an end-on view (Figure 1C) and is distinguished from the ⟨1 1 0⟩ zone by the greater number of reflections. The two perspectives unequivocally show that the lattice is oriented with the ⟨0 0 1⟩ along the length of the rod, and the ⟨1 1 0⟩ normal to the sides.[15]

These nanorods are nearly the equilibrium Wulff shape for FeF$_2$.[11,12] Oxygen substitution introduces Fe^{3+} and intercalation behavior on discharge that would complicate our mechanistic analysis.[31] The presence of any oxy-fluoride phase is excluded by x-ray diffraction (XRD) and energy dispersive x-ray spectroscopy (EDX) (Figure 1B,F). The refined c-lattice parameter from the powder XRD pattern closely matches the literature value of chemically pure FeF$_2$ (Supplementary Figure 3).[31] Additionally, EDX shows a shadow in the oxygen intensity in the area of the nanorods further indicating the absence of oxyfluoride (Figure 1F).

Electrochemical Performance in Ionic Liquid Electrolytes

The 1 m LiFSI/Pyr$_{1,3}$FSI ionic liquid (IL) electrolyte enables exceptionally stable cycling without excessive amounts of obfuscating carbon (Figure 2A,B). This advance allows for accurate observation of the intrinsic electrochemical behavior of FeF$_2$ as well as the implementation of metal fluorides in a
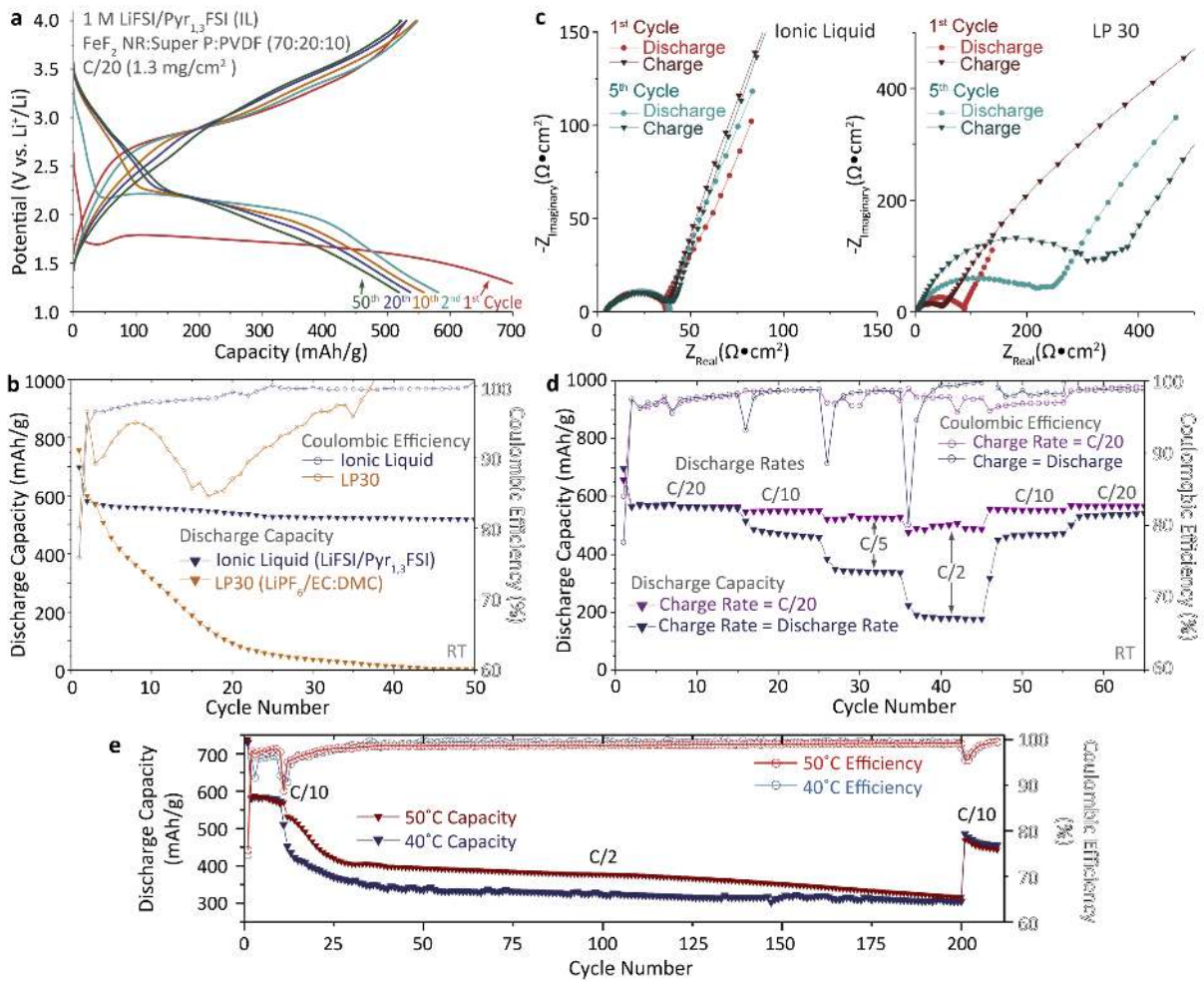
Figure 2: Electrochemical Performance. a, Galvanostatic discharge/charge profiles for various cycles of an FeF$_2$ nanorod coin cell. Charge/discharge profiles become increasingly symmetric as the number of cycles increases. **b**, Plots of discharge capacity and coulombic efficiency vs. cycle number comparing the performance of FeF$_2$ nanorod electrodes between the conventional LP30 electrolyte in orange and an ionic liquid electrolyte in purple. In the ionic liquid, more than 90% of the theoretical capacity is maintained after 50 cycles. Stability over 100 cycles is shown in Supplementary Figure 4. **c**, Nyquist impedance plots for the FeF$_2$ nanorod electrodes, demonstrating the difference in stability between the ionic liquid electrolyte (left) and the LP30 electrolyte (right). Data from the first (red) and fifth (turquoise) cycles are plotted to demonstrate the long-term effects of cycling. Impedance spectra are collected directly after discharge and charge for each cycle demonstrate significant redox activity in the LP30 derived SEI layer. Impedance spectra at the cathode and anode after prolonged cycling is shown in Supplementary Figures 5-6. **d**, Plots of discharge capacity and coulombic efficiency vs. cycle number, illustrating the rate capability of FeF$_2$ nanorod electrodes cycled in ionic liquid electrolytes. The dark purple plot shows cycling with identical discharge and charge current density. The light purple plot shows cycling with a constant charge rate of C/20 and various discharge rates. Under asymmetric conditions the discharge capacity exceeds 85% of the theoretical capacity at C/2, indicating that discharge (lithiation) kinetics are inherently much faster than charge (delithiation) kinetics. This finding is a direct result of the mechanism described herein. **e**, High rate cycling at elevated temperatures demonstrating the superior stability of the IL electrolyte.

truly energy dense format. A comparison between the IL electrolyte and a conventional 1 M LiPF$_6$ in 1:1 ethylene carbonate:dimethyl carbonate (LP30) electrolyte is made with a slow cyling rate (C/20) at room temperature (Figure 2A-C). The full breadth of the stability enabled by the IL electrolyte is shown in Figure 2E and Supplementary Figures 7-9. Stable cycling is observed for over 200 cycles at 50 °C and rates as high as C/2 (300 μA cm^{-2}).

This high temperature performance is comparable to that recently demonstrated using a solid polymer electrolyte, but is achieved at much higher active material loading (70 wt.%).[32] A direct result of our mechanistic study is the discovery that FeF$_2$ exhibits and inherently high discharge rate capability (Figure 2D).

The galvanostatic profile of FeF$_2$ nanorod electrodes (Figure 2A) shows 24% irreversible capacity

on the first discharge due to initial formation of the SEI layer. The coulombic efficiency increases immediately on the second cycle, exceeding 99% within the first 20 cycles (Figure 2B), and a stable hysteresis of 0.6 V is observed (Supplementary Figure 10). In contrast, electrodes cycled in the conventional LP30 electrolyte exhibit low coulombic efficiency, increasing hysteresis, and a total loss of capacity within the first 40 cycles (Figure 2B).

Electrochemical impedance spectroscopy (EIS) (Figure 2C) reveals virtually no increase in charge transfer resistance over the first five cycles in IL and only minimal increases thereafter, which is consistent with the stable cycling observed immediately after the first discharge. This stability is remarkable, even compared to the best electrolyte systems used in the literature, and stands in stark contrast to the rapidly increasing charge transfer resistance observed in the LP30 electrolyte.[24] In LP30 the charge transfer resistance fluctuates significantly between discharge and charge (Figure 2C). This is possibly related to the repetitive formation and partial dissolution of the SEI layer as corroborated by x-ray photoelectron spectroscopy (XPS).

XPS spectra of cycled electrodes explain the electrochemical stability of the IL-derived SEI (Figure 3C-F). XPS data for the pristine electrodes and additional elemental regions are shown in Supplementary Figures 11-16. In both electrolytes, the first discharge deposits of large amounts of aliphatic carbon with some oxygen functionalities. This phenomenon is indicated by the intense sp^3 signal in the C1s spectra and the diminishing of peaks related to Super P and PVDF and is more pronounced in LP30 (Figure 3C,D). The SEI formed from the ionic liquid contains significantly more inorganic components derived from the FSI (Figure 3H, Supplementary Figure 14 and 15). On charging, this inorganic component is increased, while the organic material becomes increasingly functionalized with nitrogen and fluorine. These additional elements may prevent the SEI from redissolving.[33,34] The IL-derived SEI is manifest in the ex-situ TEM images (Figure 3B) as an intact surface coating. This coating appears to densify with additional cycling suggesting an increasingly inorganic nature (Supplementary Figure 17). The LP30-derived SEI is completely dissolved under identical sample preparation conditions in N-methyl pyrrolidone (NMP) (Figure 3A). In LP30, Li_2CO_3 is formed on discharge but is not present after charge (Figure 3C,E); a significant portion of the organic component is also dissolved, while the concentration of $Li_4P_2O_7$ nearly doubles (Figure 3H). This redox behavior likely contributes to the low coulombic efficiency (Figure 2B).

Excessive SEI growth (Supplementary Figure 18) is a major contributor to the increasing hysteresis

and pronounced capacity fade. Additionally, XPS spectra of the Li metal anodes post-cycling show that Fe dissolution from the cathode occurs in LP30 but is prevented by the robust IL derived SEI (Supplementary Figure 19). Furthermore, a third mechanism is clearly present in the fusing of the FeF_2 nanorods during discharge. Large irregular particles appear immediately after the first discharge (Figure 3A). This rapidly increases the particle size beyond the length-scale of the reconversion reaction, leaving effectively dead material at the center.[7,14] In-situ TEM measurements in the absence of electrolyte (Supplementary Video 1) showcase the propagation of the reaction front across interparticle boundaries such that two nanorods appear to react as one (Figure 3G). This phenomenon was not observed in the IL electrolyte (Figure 3B). It's possible that electrostatic interaction between the IL and FeF_2 surface creates a strongly bound solvation layer, effectively separating the particles during cycling.[35] In any case, the monodispersity and morphology of the nanorods is maintained during cycling, enabling definitive mechanistic conclusions.

The Comprehensive Conversion Mechanism

The Ex-situ HRTEM data presented in Figure 4 depicts the conversion reaction with an unprecedented level of detail. Different reaction stages are referenced between galvanostat (Figure 4A), XRD (Figure 4B), and HRTEM (Figure 4C) using the numbers 0-7 (i.e. Figure 4A-1). Non-destructive sample preparation is described in the Methods section. In-situ TEM measurements require a large negative bias between the lithium probe and the sample, which promotes kinetic reaction pathways, making it difficult or impossible to observe transient intermediates that are stable in a real battery.[36,37] Nevertheless, we employ in-situ TEM to help visualize and corroborate larger scale observations from the ex-situ data (Supplementary Video 2, 3). Enlarged TEM images, inverted contrast FFTs, and simulated diffraction patterns for each sample are shown in Supplementary Figures 20-28. EELS measurements are shown in Supplementary Figures 29-32 and Extended Data Fig. 1-3.

Surface Reactions

Reversible metal fluoride systems are invariably defined by particle sizes in the tens of nanometers and correspondingly high surface areas.[7,25,26,28] Despite being necessarily substantial, reactions specific to the surface have been largely ignored in the investigation of transition metal fluorides. The FeF_2 surface exhibits a distinct direct conversion reaction that plays a critical role in defining the reaction mechanism of the bulk. The reaction be-
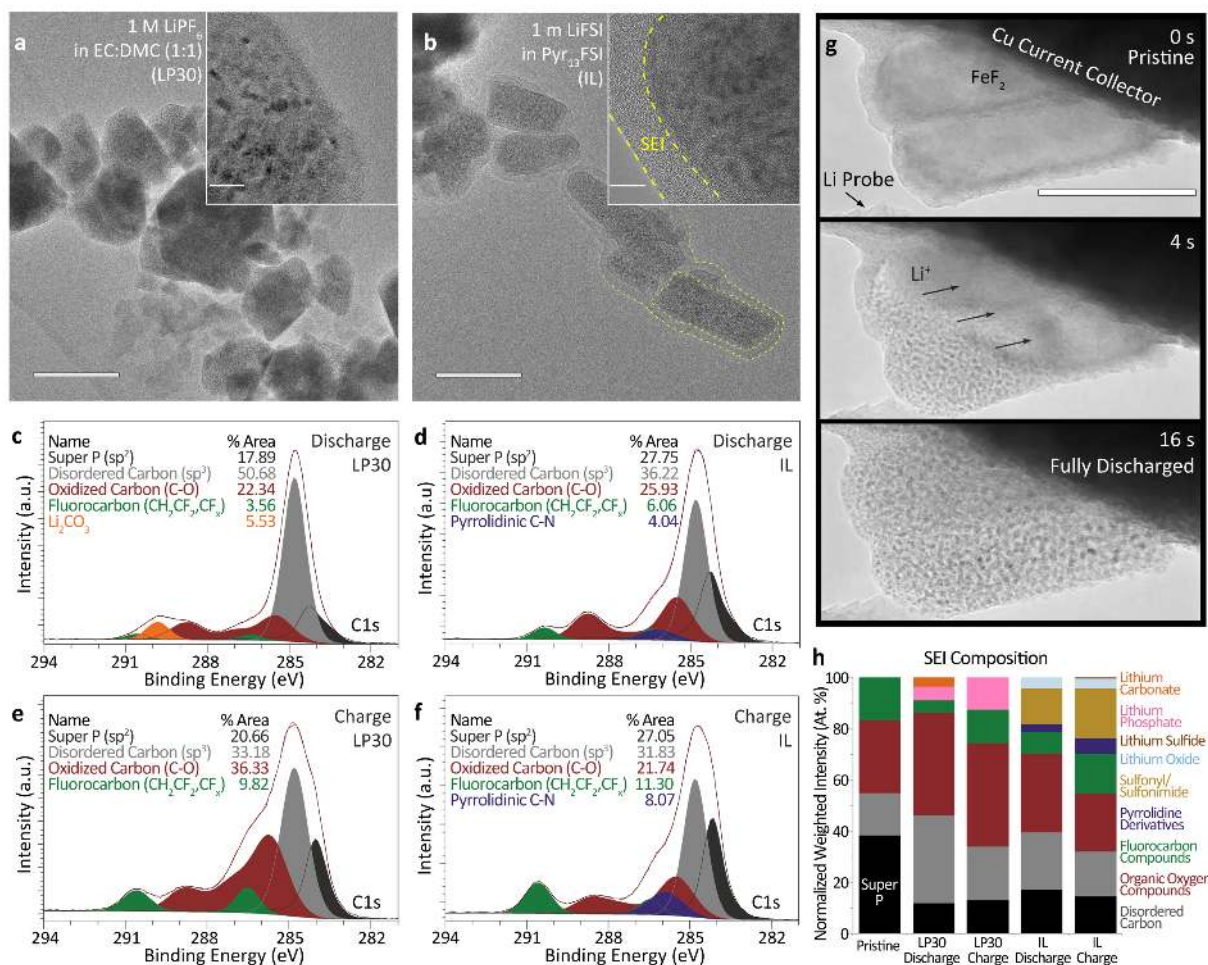
Figure 3: Electrolyte Effects. a, b, Ex-situ TEM micrographs of FeF$_2$ nanorods after a single discharge in LP30 (**a**) and IL (**b**) electrolytes. The exclusive presence of large irregular particles in (**a**) showcases a major failure mechanism in the fusing of adjacent nanorods. (**b**) Shows that fusing of particles is largely prevented in the IL electrolyte. Insets show high-magnification images of the nanoparticle periphery, an obvious SEI layer is absent from (**a**) and is likely removed during sample preparation. The ~10 nm thick surface layer shown in B indicates lower solubility of the IL-derived SEI in organic electrolytes. **c, e** C1s XPS spectra of FeF$_2$ nanorod electrodes cycled in LP30 electrolyte, demonstrating the formation of a significant aliphatic layer on discharge (**c**) and its dissolution on charge (**e**); see also Supplementary Figures 12 and 13. **d, f**, C1s spectra of electrodes cycled in IL electrolyte; a less massive aliphatic layer observed on discharge (**d**), and an increase in N and F functionalities is observed on charge (**f**). **g**, TEM micrographs extracted from an in-situ lithiation (discharge) experiment, illustrating the fusing of adjacent FeF$_2$ particles. Prior to lithiation (top), a distinct boundary is apparent between the two nanorods. During the lithiation (middle), propagation of the reaction front from one rod to the next obscures the boundary. In the fully discharged state (bottom), the boundary is no longer apparent. **h**, Chart summarizing the XPS-derived surface composition for samples in (**c-f**). Each component is derived from deconvoluted high resolution spectra weighted by their abundance in the survey spectrum. This calculation is illustrated in Supplementary Figure 16. Scale bars, 200 nm (**a,b**), 10 nm (**a,b** inset), 50 nm (**g**)

gins at the equilibrium discharge potential for FeF$_2$, 2.6 V vs. Li$^+$/Li, (Figure 4A-0) with a small capacity ($<5\%$) observed directly before the activation overpotential (Figure 4A-1). This corresponds to the formation of a disordered surface layer (2 to 4 nm) of finely divided reaction products (Figure 4C-1, Supplementary Figure 20). This layer is distinguished from the SEI by short-range (<2 nm) lattice fringes and strong Fe^0 EELS signal (Supplementary Figure 31). The structure of this layer is reminiscent of that predicted by Ma and Garofalini

using a molecular dynamics approach.[11] The mechanism for its formation may indeed follow a similar pathway, whereby the insertion of lithium within the first few atomic layers causes a disordering of the lattice and the rapid formation of exceedingly small iron clusters. The prediction of anisotropic behavior along different crystallographic directions is also confirmed.[11] Along the [0 0 1] direction, the interface between the amorphous layer and the single crystal is diffuse, suggesting short-range intercalation quickly followed by conversion; conversely,

along the $[1\,1\,0]$ direction, the interface appears sharp, suggesting a layer by layer process (Figure 4 C-1).

This direct conversion is limited to the first few nanometers of material, as the reaction model requires an uninhibited supply of electrons to the reaction front.[11] This assumption breaks down a small distance away from the Super P at the surface. Lithium diffusion kinetics also decrease considerably as the converted layer grows to even a few nanometers.[11] This is reflected in the rapid drop in cell potential observed in the galvanostatic profile (Figure 4A-0,1).[38] Ultimately, it is the diminished electron transport beyond the surface that necessitates a different reaction mechanism within the bulk. However, lithium diffusion within the bulk is defined by the formation and growth of this surface layer.

The initial finely divided surface layer is energetically unfavorable, and as discharge progresses, the crystallinity of this layer increases with the phase segregation of Fe and LiF (Figure 4C-2, Supplementary Figures 21 and 33). By Stage 3, a strikingly epitaxial, crystalline double-layered shell has formed with a light layer of LiF around the core of the particle, further encapsulated by a dark layer of metallic iron (Figure 4C-3, Supplementary Figures 22 and 23). Accordingly, EELS measurements show that iron signal is spatially offset toward the surface from the fluorine signal (Supplementary Figure 30). The $LiF|FeF_2$ interface is fully coherent and the arrangement of layers $Fe|LiF|FeF_2$ minimizes the total interfacial free energy.

The insertion of Li^+ into a crystalline LiF or Fe surface is energetically and mechanistically not possible.[12] As the double-layered shell forms primarily on the $\{1\,1\,0\}_{FeF_2}$ facets, the sides of the nanorod are rendered impermeable to lithium at an early stage in the reaction. This phenomenon, combined with the low energy barrier for diffusion along the $\langle 0\,0\,1 \rangle_{FeF_2}$ direction forces lithiation to proceed in a unidirectional fashion along the length of the nanorod (Figure 4C-3, Supplementary Figures 25 and 26).[11] The $Fe|LiF$ double-layered shell remains largely unchanged throughout the discharge.

The delithiation reaction requires the diffusion of lithium out of the nanorod and the concomitant insertion of iron into the LiF lattice. Lithium in the double-layered shell cannot diffuse outward through the iron, and the iron cannot easily migrate across the semi-coherent interface into the LiF (Figure 4C-5, Supplementary Figures 25 and 26).[39] It is only at a nearly fully charged state that the double-layered shell disappears (Figure 4C-6, Supplementary Figure 27). Coincidentally, the shell becomes amorphous once again, eliminating the semi-coherent $LiF|Fe$ interface. However a large overpotential is required for this amorphiza-

tion, and this reconversion of the double-layered shell does not occur until 3.3 V vs. Li^+/Li (Figure 4A-5), which is above the reduction potential for $Fe^{3+} \rightarrow Fe^0$ (3.0 V vs. Li^+/Li).[40] In systems without a stable SEI layer, or equivalent, dissolution of the metal shell is preferred, leading to eventual cell failure.[24,27]

Pseudo Intercalation and the Activation Overpotential

It is frequently assumed that the activation overpotential observed on the first discharge (Figure 4A-1) is related to the initial nucleation and growth of Fe^0 and LiF grains, in other words, the onset of conversion.[5,14,18,19] This is actually a misconception; the true origin of the activation overpotential is the formation of a second phase via the disproportionation of iron and pseudo-intercalation of lithium within the nanorod interior.

After the dip in potential (Figure 4C-2) the nanorods appear morphologically unchanged from the previous stage (Figure 4C-1). However, a FFT derived from the interior of the nanorods (Figure 4C-2, Supplementary Figure 21) exhibits several sets of reflections: one from the $\langle 1\,1\,0 \rangle$ zone of FeF_2 and a second set with larger d-spacings that is unambiguosly indexed to the $\langle 1\,1\,0 \rangle$ zone of the trirutile $LiFe_2F_6$.[21,41] The trirutile reflections share the same symmetry and $\langle 0\,0\,1 \rangle$ direction as those of the FeF_2, indicating an identical lattice orientation. This is consistent with the fully coherent structure observed in the TEM (Figure 4C-2). Unsurprisingly, conventional powder XRD shows little change (Figure 4B-1,2) as most major reflections from this trirutile phase overlap those of FeF_2.[41] The structure of the trirutile phase is practically identical to that of FeF_2 with lithium periodically substituted for iron (Figure 5D). The formation of this phase can be visualized as the Li^+ diffusing through the channels in the $[0\,0\,1]_{FeF_2}$ direction before knocking an iron cation out of a lattice site. A concomitant reduction of Fe^{2+} to Fe^+ or a disproportionation ($Li^+ + 3\,Fe^{II}F_2 + e^- \rightarrow LiFe^{II}Fe^{III}F_6 + Fe^0$) is required to accommodate the Li^+.[21] Disproportionation must also produce Fe^{3+} cations;[20,21] indeed, EELS measurements at this stage reveal a splitting of the Fe L_3 peak toward higher energy loss values indicative of Fe^{3+} species (Extended Data Fig. 1).[42] Doe et al. predicted this trirutile phase as an equilibrium intermediate in the conversion of iron fluorides over a decade ago.[21] Experimental validation is finally achieved through the pairing of real battery conditions with the high resolution structural data afforded by monodisperse, single-crystalline nanoparticles.

A true intercalation via wholesale reduction of Fe^{2+} to Fe^+ is not allowed; however, the lithium diffusion barrier in the $\langle 0\,0\,1 \rangle_{FeF_2}$ is low.[11,20,21]
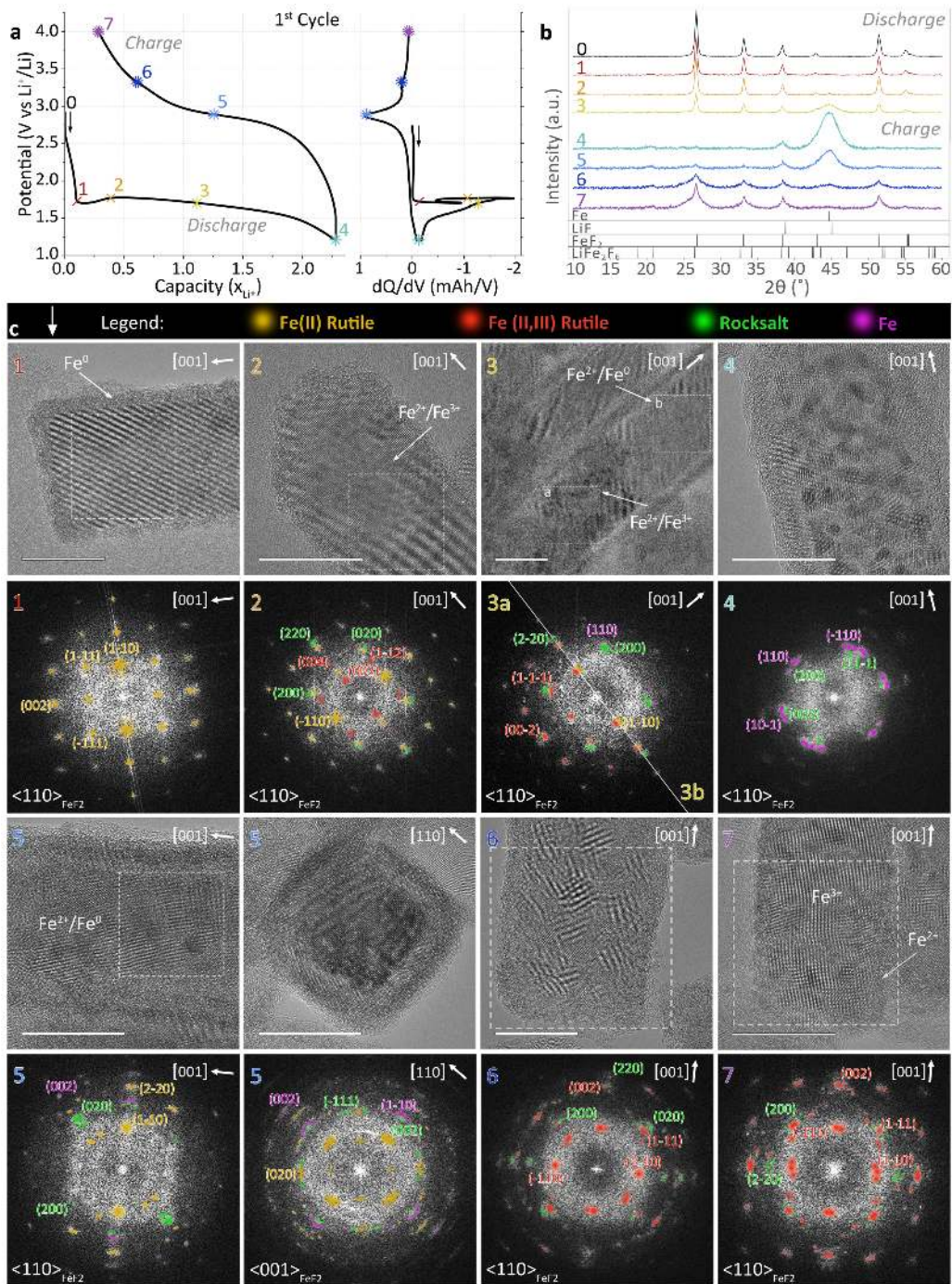
Figure 4: Ex-situ XRD and HRTEM. a, The galvanostatic profile and corresponding dQ/dV for the first discharge/charge cycle plotted with the same "Potential" axis to highlight the position of major electrochemical processes. Ex-situ data points (XRD, TEM) are indicated by numbers 0-7 and corresponding color-coded markers. **b**, Powder XRD patterns of the ex-situ samples denoted in (**a**). Discharge patterns (top) show a gradual decrease in FeF_2 intensity and the concomitant formation of rocksalt followed by Fe^0. A small LiF peak and broad Fe peak are apparent in the fully discharged state. Upon charging (bottom), the Fe peaks are diminished and replaced by a set of broad rutile peaks. **c**, Ex-situ HRTEM micrographs and corresponding FFT patterns for samples 1-7. Images for each sample are captured along the $\langle 1\,1\,0 \rangle_{FeF_2}$ zone axis, the common $[0\,0\,1]$ direction is indicated in the top right of each panel. A second image along the $\langle 0\,0\,1 \rangle_{FeF_2}$ zone axis is shown for sample 5 to showcase the orientation relationship in the double-layered shell and the persistence of the square cross-section. Diffraction spots are selective colored using white pixel intensity according to the legend displayed in the top bar. Fe oxidation states are determined by EELS (Supplementary Figures 29-32, Extended Data Figs. 1-3). Dotted white boxes denote the areas over which the FFT has been taken; when absent, the FFT has been taken over the whole image. All FFT patterns are set to the same scale. Scale bars, 20 nm. A full step-by-step description of the HRTEM/EELS data is provided in Supplementary Figures 20-28. 1) 1.7 V, $x_{Li+} = 0.05$. 2) 1.75 V, $x_{Li+} = 0.3$. 3) 1.7 V, $x_{Li+} = 1.0$. 4) 1.2 V, $x_{Li+} = 2.0$. 5) 2.9 V, $x_{Li+} = 1.0$. 6) 3.3 V, $x_{Li+} = 0.3$. 7) 4.0 V, $x_{Li+} = 0.0$.

Thus a pseudo-intercalation occurs with an activation overpotential required to initiate disproportionation (Figure 4A-1). A brief discussion of possible charge transport mechanisms is provided with Supplementary Figure 21. The conventional description of discharge as a three-phase reaction between FeF_2, LiF, and Fe is clearly incorrect and fails to capture the complex phase equilibria present in a reversible metal fluoride system.

Phase Equilibria and Reaction Symmetry

Several studies have suggested that phase evolution in transition metal difluorides follows different chemical pathways for discharge and charge.[5,14,19] However, the presence of structurally similar reaction intermediates and different mechanisms between the surface and the bulk can confound the interpretation of spectroscopic data. With a high degree of spatial resolution, we show the local evolution of phases is remarkably symmetrical between charge and discharge, differing not in the spatial distribution of phases, but in the temporal separation of different reaction steps.

In addition to reflections from FeF_2 and trirutile phases, nanorods during Stage 2 of discharge exhibit a set of reflections from the $\langle 0\,0\,1 \rangle$ zone of a rocksalt phase (Figure 4C-2, Supplementary Figure 21). The relatively high intensity of these reflections and the appearance of the $\{2\,0\,0\}$ rocksalt peak in the powder XRD (Figure 4B-2) suggests an Fe substituted rocksalt phase with an increased structure factor similar to that reported by Ko et $al.$[5,14,19] The rocksalt arises from the decomposition of unstable phases formed from Li^+ intercalation beyond the $LiFe_2F_6$ stoichiometry.[21,41] Disregarding the double-layer shell, an initial "unconverted" equilibrium exists between FeF_2, rutile $Li_yFe_{3-y}F_6$, and rocksalt $Fe_zLi_{2-z}F_2$.

Inevitably, a second "converted" equilibrium emerges as further lithiation consumes native FeF_2 and increasing Fe^0 concentration nucleates metallic Fe particles. Astonishingly, in the 50% discharged state, both the unconverted (Figure 4C-3a, Supplementary Figure 22) and converted (Figure 4C-3b, Supplementary Figure 23) regimes exist simultaneously in each nanorod with a distinct boundary perpendicular to the $[0\,0\,1]_{FeF_2}$ direction. The converted section is marked by the appearance of discreet Fe nanoparticles, while the unconverted section is defined by presence of higher index FeF_2 reflections. Equivalently, an EELS line scan along the $[0\,0\,1]_{FeF_2}$ direction (Supplementary Figure 29) shows a sharp transition from a converted area of Fe^{2+} and Fe^0 to an unconverted area containing Fe^{2+} and Fe^{3+} (Figure 4C-3 overlay). FFT of the converted region indicates a three-phase equilibrium with clear Fe^0 and rocksalt $Fe_zLi_{2-z}F_2$

reflections and weak rutile $Li_yFe_{3-y}F_6$ reflections.

On charging (delithiation), the "converted" and "unconverted" equilibria are observed separately over two distinct plateaus (Figure 4A-5,6). The first plateau at 2.9 V vs. Li^+/Li (Figure 4A-5) occurs close to the 50% charged state; however, no distinct conversion boundary is observed (Figure 4C-5, Supplementary Figure 25). Compared to the fully discharged state (Figure 4C-4, Supplementary Figure 24), an FFT from the first plateau (Figure 4C-5) exhibits an increased intensity of rocksalt reflections as Fe is substituted into the LiF lattice. Ko et $al.$ demonstrated the stability of this rocksalt $Fe_zLi_{2-z}F_2$ phase up to a composition of z = 0.5.[14] Accordingly the reappearance of a rutile $Li_yFe_{3-y}F_6$ phase is also confirmed by FFT at x_{Li^+} = 1.0. Distinct iron particles are visible and EELS spectra indicate the presence of Fe^{2+}/Fe^0 species (Supplementary Figure 32), recreating the phase relationship and appearance of the converted section of the nanorod from Stage 3 of discharge (Figure 4C-3a).

The second plateau at 3.3 V vs. Li^+/Li (Figure 4A-6) occurs after the complete consumption of Fe particles in the interior of the nanorod, as demonstrated by the near complete disappearance of the broad Fe peak in the XRD pattern (Figure 4B-6). FFT of HRTEM images from this plateau show decreased intensity of rocksalt reflections and the reappearance of higher index rutile reflections (Figure 4C-6, Supplementary Figure 27). Interestingly, this second plateau also corresponds with the further oxidation of Fe^{2+} species. EELS spectra of the fully recharged state (Extended Data Fig. 3) show an additional peak and the higher L_3 position characteristic of Fe^{3+}. The kinetically limited insertion of Fe from the outer shell, relegates the coherent LiF/rutile core to reconvert with a stoichiometry closer to FeF_3. Accordingly, EELS spectra from the reconverted shell indicate the presence of Fe^{2+}, with residual metallic Fe visible in the bright field TEM (Figure 4C-7, Extended Data Fig. 3). This Fe^{3+} formation explains how the potential plateau around 3.3 V appears on and after the second discharge cycle. Thus, the phase equilibria present during this second plateau mirrors that of the unconverted portion of the nanorod during Stage 3 of discharge (Figure 4C-3b) in both crystal structure and oxidation state. The reaction pathways are chemically symmetric to a large extent; the discharge and charge profiles also become increasingly symmetric with each successive cycle. A disparate arrangement of electrochemically active species on discharge and charge is thought to contribute to voltage hysteresis.[18] However, this "compositional inhomogeneity" is not apparent for FeF_2 as the spatial distribution of phases on charge and discharge is also largely symmetric. The large hysteresis ob-
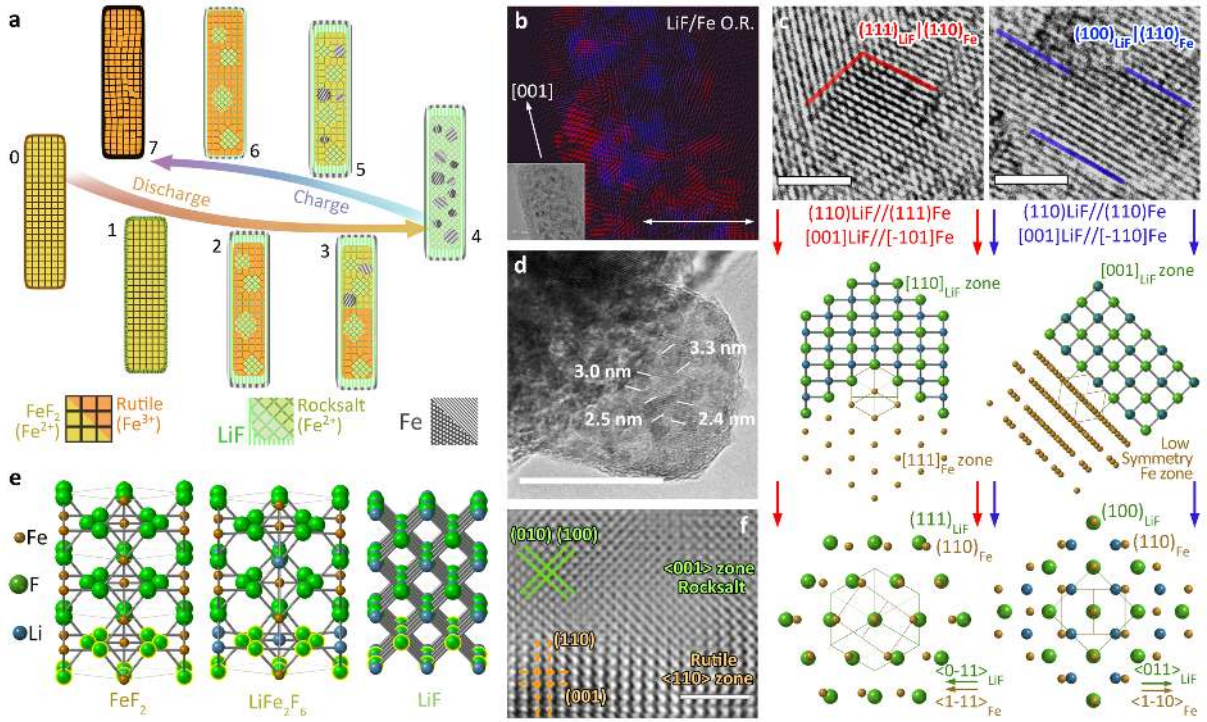
Figure 5: Conversion Mechanism. a, Schematic of the full discharge/charge mechanism representing the ex-situ data points (0-7). Direct conversion at the surface forms disordered Fe|LiF (1), after which coherent trirutile and rocksalt phases are formed throughout the interior with the concomitant formation of a double-layered Fe|LiF shell (2). The shell limits the propagation of the reaction to the [0 0 1], creating a boundary between the converted (iron containing) and unconverted regions (3). The fully discharged state contains iron particles nucleated on low-energy interfaces within the fluoride matrix (4), charging proceeds with the consumption of these iron particles (5), the reconversion of the double-layered shell (6), and the reformation of a pseudo single-crystalline rutile nanorod. **b**, Composite IFFT image showing spatial distribution of type I (red) and type II (blue) orientation relationships in the fully discharged state. **c** Magnified TEM images (top) of single Fe nanoparticles and surrounding LiF exhibiting type I (left) and type II (right) orientation relationships. Colored lines demarcate the planar, semi-coherent interfaces. (Middle) Crystal models recreating the above orientation relationships. (Bottom) Superposition of interface atoms describing the lattice matching at the semi-coherent interfaces. **d**, Frame extracted from an in-situ lithiation experiment showing the formation of iron nanoparticles with an initial diameter of $\sim$3 nm (Supplementary Video 3). Contact with the lithium probe occurs out of frame. **e**, Crystal models of FeF_2, $LiFe_2F_6$ and LiF arranged with empirically observed orientation relationships to illustrate the invariant fluoride lattice. Equivalent fluorine atoms are highlighted in yellow. **f**, IFFT image of the interface between the rutile core and the rocksalt shell that exemplifies the orientation relationship and lattice coherency between the two phases. Scale bars, 20 nm (**b,d**), 2 nm (**f,c**).

served in metal fluorides may primarily be a result of the internal resistance and the reaction overpotential, which are more easily mitigated by rational electrode/materials design.

The Invariant Fluoride Lattice

The lattice orientation relationship (O.R.) between FeF_2, rutile, rocksalt and LiF reveals that conversion proceeds with nearly universal coherency between fluoride phases, resulting from invariant lattice of fluoride anions (Figure 5E,F). This new discovery may present the single greatest rationale for the reversibility of the conversion reaction iron fluoride and similar transition metal difluorides. Lattice orientation is naturally maintained in transformations between phases with the same

crystal structure (i.e. FeF_2/rutile or LiF|rocksalt). Additionally, a ubiquitous alignment between the $\{2\,0\,0\}$ reflections from the $\langle 0\,0\,1 \rangle_{rocksalt/LiF}$ zone and the $\{1\,\bar{1}\,\bar{1}\}$ reflections from the $\langle 1\,1\,0 \rangle_{rutile|FeF_2}$ zone (Figure 4C-2–7) defines the orientation relationship $(1\,1\,0)_{rutile}//(0\,0\,1)_{rocksalt}$, $[1\,\bar{1}\,0]_{rutile}//[1\,\bar{1}\,0]_{rocksalt}$ (Figure 5E, Table 1). This relationship is visible at the periphery of the nanorod (Figure 5F). The $(1\,1\,0)_{rutile}//(1\text{-}10)_{rocksalt}$, $[1\,\bar{1}\,0]_{rutile}//[0\,0\,\bar{1}]_{rocksalt}$ relationship symmetrically equivalent by 90° rotation about the $[0\,0\,1]_{FeF_2}$ nanorod axis is also present. Superposition of the two lattices with this relationship reveals that the arrangement of fluoride ions is nearly identical (Figure 5E). The decomposition of the rutile to form rocksalt involves the insertion lithium at inter-

10

stitial sites within the $[0\,0\,1]_{rutile}$ channels, followed by the shifting of cations at the body center. The transformation $FeF_2 \rightarrow rutile \rightarrow rocksalt \rightarrow LiF$ is an entirely topotactic transformation involving intercalation and diffusion of cations within a stable fluoride host.

The reverse topotactic transformation is observed on charge with the exact same orientation relationship. However, delithiation requires migration of the fluoride interface into regions of iron and amorphous material. The formation of this new fluoride material occasionally results in FeF_2 grains rotated from the original lattice orientation (Figure 4C-5–7, Supplementary Figures 25-28). In the fully recharged state the crystal structure and lattice orientation of the original nanorod are almost entirely restored, resulting in the reformation of a pseudo-single crystalline nanorod morphology (Figure 4C-7, Supplementary Figure 28). This stunning manifestation of reversibility is further displayed as the nanorod morphology is actually maintained for over 50 discharge/charge cycles (Supplementary Figure 34). The shared orientation of the metallic iron particles on discharge is a secondary effect of the invariant fluoride lattice. Orientation relationships between all phases are summarized in Table 1.

Iron Particle Orientation

On discharge, distinct iron particles are not observed until lithium insertion to half the theoretical capacity, and even at this stage they are sparsely distributed within the converted section of the nanorod (Figure 4C-3b). Likewise XRD, shows a low-intensity, broad $\{1\,1\,0\}_{Fe}$ reflection (Figure 4B-3). This delayed nucleation of iron particles likely results from the interfacial free energy cost between the iron and the fluoride lattice. This activation energy barrier results in a corresponding critical radius and Fe^0 concentration below which nucleation of iron particles cannot occur.[39] Indeed, in-situ measurements depict iron particles forming with an initial diameter of 2 to 3 nm (Figure 5D, Supplementary Video 3). The first particles to form on discharge do not appear to be well connected, suggesting they are not crucial for electron conduction as previously thought. Similarly, the iron particles are one of the first features to disappear on charging (Figure 4C-5, Supplementary Figure 25). Nevertheless, the orientation of these metallic nanoparticles with respect to the fluoride lattice is well defined and has large implications for the kinetics and reversibility of the reaction.

In the fully discharged state (Figure 4C-4), the original $\langle 1\,1\,0 \rangle_{FeF_2}$ zone axis orientation can be identified by the symmetry of the LiF reflections on the basis of the invariant fluoride lattice. Despite the two-phase polycrystalline nature of this stage,

the FFT along this zone axis is astonishingly symmetrical, displaying reflections from the $\langle 1\,0\,0 \rangle_{LiF}$ and $\langle 1\,1\,0 \rangle_{LiF}$ zones and several different iron zones, predominantly the $\langle 1\,1\,1 \rangle_{Fe}$ (Figure 4C-4). The $\{0\,0\,2\}_{LiF}$ reflections of the $\langle 1\,1\,0 \rangle_{LiF}$ zone are entirely coincident with the $\{1\,\bar{1}\,0\}_{Fe}$ reflections from the $\langle 1\,1\,1 \rangle_{Fe}$ zone, resulting in the orientation relationship $(1\,1\,0)_{LiF}//(1\,1\,1)_{Fe}$, $[0\,0\,1]_{LiF}//[\bar{1}\,0\,1]_{Fe}$ (type I – Table 1, Figure 5C red). Reflections from the $\langle 1\,1\,0 \rangle_{Fe}$ zone are also present as dictated by the four-fold rotational symmetry of the nanorod.

A second orientation relationship is apparent as the $\{2\,0\,0\}$ and $\{0\,2\,0\}$ reflections from the $\langle 1\,0\,0 \rangle_{LiF}$ zone are entirely coincident with the $\{1\,1\,0\}_{Fe}$ reflections from a lower symmetry orientation (Figure 4C-4, Supplementary Figure 24). Comparison with the orientation of Fe in the double-layered shell (Figure 4C-5) reveals the relationship $(1\,1\,0)_{LiF}//(1\,1\,0)_{Fe}$, $[0\,0\,1]_{LiF}//[-1\,1\,0]_{Fe}$ (type II – Table 1, Figure 5C blue). An inverse FFT demonstrates that the two orientation relationships are mutually exclusive in space, indicating that the orientation of the iron particles is defined by that of the surrounding LiF (Figure 5B). Closer examination of the iron nanoparticles reveals that they are truncated ellipsoids with exposed facets that share a planar interface with the LiF matrix (Figure 5C). Iron nanoparticles are preferentially nucleated on low energy interfaces within the coherent fluoride matrix, corroborating the presence a significant interfacial free energy barrier to nucleation. Lattice matching at these interfaces defines the orientation of the iron nanoparticles with respect to the nanorod.

For type I particles, the $\{1\,\bar{1}\,1\}_{LiF}|\{1\,1\,0\}_{Fe}$ interface is dominant. Based on the orientation relationship, lattice matching between the $\{1\,\bar{1}\,1\}_{LiF}$ and $\{1\,1\,0\}_{Fe}$ and occurs such that $\langle 0\,\bar{1}\,1 \rangle_{LiF}//\langle 1\,\bar{1}\,1 \rangle_{Fe}$ (Figure 5C). This is exactly the Kurdjumov-Sachs interface that occurs in many FCC|BCC systems.[39,43] In the case of type II particles, the $\{1\,0\,0\}_{LiF}|\{1\,1\,0\}_{Fe}$ interface is dominant and the orientation relationship dictates that $\langle 1\,1\,0 \rangle_{LiF}//\langle 0\,1\,1 \rangle_{Fe}$ (Figure 5C). At this interface, the $\{0\,1\,1\}_{LiF}$ spacings are matched to the $\{0\,1\,1\}_{Fe}$ spacings with a difference of only 2.6 pm; this particular interface was actually calculated to be the lowest energy interface involving the $\{0\,0\,1\}_{LiF}$ plane.[12] While these low energy semi-coherent interfaces are crucial for the nucleation of small iron nuclei on discharge, it is the higher energy curved interfaces, which enable the consumption of iron particles on charge. The transfer of an Fe atom across a coherent interface requires a statistically unlikely vacancy on the opposite side.[39] The transfer of atoms across high-energy interfaces is far more probable and facilitates diffusion of iron back into the fluoride lattice. The

Phase Name	Parallel Lattice Plane (hkl) and Direction [uvw]		
FeF_2 (rutile)	Side View: $(1\,1\,0),[1\,\bar{1}\,0]$		Top View: $(0\,0\,1),[1\,1\,0]$
LiF (rocksalt)	$(1\,0\,0),[0\,0\,\bar{1}]$	$(0\,0\,1),[0\,1\,0]$	$(1\,1\,0),[0\,0\,\bar{1}]$
Fe	$(1\,1\,1),[1\,0\,\bar{1}]$	$(\overline{0.174}\,0.174\,0.147),[1\,1\,0]$	$(1\,1\,0),[1\,\bar{1}\,0]$
Label	Type I	Type II	

Table 1: Orientation Relationships summarized as columns of parallel planes and directions.

only iron particles that remain at stage 5 of charge exhibit large areas of coherent interface (Figure 4C-5).

In a reversible system, the removal of lithium without replacement by another cation would leave an uncompensated F^-, which is energetically unfavorable. Thus lithium can only be extracted as fast as it can be replaced by iron. The delithiation is thus limited by the rate at which iron atoms can be transported across the Fe|LiF interface, that is, charging is interface controlled. In contrast, insertion of lithium from the electrolyte is fast and the discharge reaction is diffusion controlled. This concept is partially responsible for the disparity in discharge and charge kinetics demonstrated in Figure 2D. As thermal energy increases, a greater proportion of iron atoms are able to jump accross the Fe|LiF interface, ultimately resulting in the improved rate capability observed at higher temperatures.

Nanorod morphology is preserved over many cycles (Extended Data Fig. 4). A discussion of how this occurs is included with Supplementary Figure 34.

The colloidal synthesis of single crystalline, monodisperse FeF_2 nanorods holds immense value, not only for electrochemical performance, but also mechanistic understanding. The full potential of this system is achieved when combined with the $LiFSI/Pyr_{1,3}FSI$ ionic liquid electrolyte, which prevents the fusing of particles during cycling, allowing for accurate assessment of morphological and structural transformations. The ability of this IL electrolyte to enable reversible cycling without the use of impractical carbon scaffolds or the introduction of otherwise inactive material is paramount to the realization of high energy density transition metal fluoride LIBs.

From the unparalleled vantage point of the FeF_2 nanorods, HRTEM unearths new concepts governing the conversion reaction in transition metal fluorides, namely the direct conversion and phase segregation localized to the surface, the topotactic evolution of coherent phases based an invariant fluoride lattice, and the nucleation and lattice matching of metallic particles on semi-coherent interfaces. In developing this new understanding, we have answered long-standing questions regarding the possibility of intercalation, role of metallic

iron, the asymmetry of the reaction pathway, and the validity of computed reaction intermediates and mechanistic models. The abundance and specificity of these results highlights the utility of monodisperse, single crystalline nanoparticle methods for the mechanistic study of electrode systems in general.

The comprehensive conversion mechanism detailed here reveals that the charge reaction is interface controlled, accompanied by the slow diffusion of Fe^{2+} through a rocksalt lattice and is thus inherently sluggish. In contrast, the discharge reaction is diffusion controlled and accompanied by the fast diffusion of Fe^0 through open channels in the $\langle 0\,0\,1\rangle_{FeF_2}$ direction.[15] An excellent discharge rate capability can be achieved as long as the rate of charge is slow enough to recover the full capacity (Figure 2D), implying the suitability of transition metal fluoride cathodes for applications such as electric aircraft. Charge and discharge pathways are spatially and chemically symmetric, suggesting that voltage hysteresis is primarily a result of the reaction overpotential. Thus, the reaction hysteresis could potentially be mitigated through materials design, for example doping or structural control. In tetragonal systems, surface metal, which is prone to dissolution, forms primarily on the $\{1\,1\,0\}_{rutile}$ surface, while net Li^+ diffusion is limited to the $\langle 0\,0\,1\rangle_{rutile}$ direction. Thus minimization of the $\{1\,1\,0\}$ surface would improve both reversibility and reaction kinetics.

References

1. Schäfer, A. W. *et al.* Technological, economic and environmental prospects of all-electric aircraft. *Nature Energy* **4**, 160–166 (2019).

2. Janek, J. & Zeier, W. G. A solid future for battery development. *Nature Energy* **1**, 16141 (2016).

3. Choi, J. W. & Aurbach, D. Promise and reality of post-lithium-ion batteries with high energy densities. *Nature Reviews Materials* **1** (2016).

4. Li, H., Balaya, P. & Maier, J. Li-Storage via Heterogeneous Reaction in Selected Binary Metal Fluorides and Oxides. *Journal of The Electrochemical Society* **151**, A1878 (2004).

5. Li, C., Chen, K., Zhou, X. & Maier, J. Electrochemically driven conversion reaction in fluoride electrodes for energy storage devices. *npj Computational Materials* **4** (2018).

6. Amatucci, G. G. & Pereira, N. Fluoride based electrode materials for advanced energy storage devices (2007).

7. Badway, F., Cosandey, F., Pereira, N. & Amatucci, G. G. Carbon Metal Fluoride Nanocomposites. *Journal of The Electrochemical Society* **150**, A1318 (2003).

8. Zhang, N., Xiao, X. & Pang, H. Transition metal (Fe, Co, Ni) fluoride-based materials for electrochemical energy storage. *Nanoscale Horizons* **4**, 99–116 (2019).

9. Bruce, P. G., Scrosati, B. & Tarascon, J.-M. Nanomaterials for rechargeable lithium batteries. *Angew. Chem. Int. Ed.* **47**, 2930–2946 (2008).

10. Liu, C., Neale, Z. G. & Cao, G. Understanding electrochemical potentials of cathode materials in rechargeable batteries. *Materials Today* **19**, 109–123 (2016).

11. Ma, Y. & Garofalini, S. H. Atomistic insights into the conversion reaction in iron fluoride: A dynamically adaptive force field approach. *Journal of the American Chemical Society* **134**, 8205–8211 (2012).

12. Ma, Y. & Garofalini, S. H. Interplay between the ionic and electronic transport and its effects on the reaction pattern during the electrochemical conversion in an FeF2 nanoparticle. *Physical Chemistry Chemical Physics* **16**, 11690–11697 (2014).

13. Wang, F. *et al.* Ionic and Electronic Transport in Metal Fluoride Conversion Electrodes. *ECS Transactions* **50**, 19–25 (2013).

14. Ko, J. K. *et al.* Transport, phase reactions, and hysteresis of iron fluoride and oxyfluoride conversion electrode materials for lithium batteries. *ACS Applied Materials and Interfaces* **6**, 10858–10869 (2014).

15. Karki, K. *et al.* Revisiting Conversion Reaction Mechanisms in Lithium Batteries: Lithiation-Driven Topotactic Transformation in FeF2. *Journal of the American Chemical Society* **140**, 17915–17922 (2018).

16. Wang, F. *et al.* Tracking lithium transport and electrochemical reactions in nanoparticles. *Nature Communications* **3**, 1201–1208 (2012).

17. Chuan-zheng, Y., Jian-min, H. A. O. & Guang-wen, P. E. I. Contributed Papers Brief Introduction of X-Ray Multiple Diffraction. *The Rigaku Journal* **17**, 46–57 (2000).

18. Li, L. *et al.* Origins of Large Voltage Hysteresis in High-Energy-Density Metal Fluoride Lithium-Ion Battery Conversion Electrodes. *Journal of the American Chemical Society* **138**, 2838–2848 (2016).

19. Wang, F. *et al.* Conversion reaction mechanisms in lithium ion batteries: Study of the binary metal fluoride electrodes. *Journal of the American Chemical Society* **133**, 18828–18836 (2011).

20. Yamakawa, N., Jiang, M., Key, B. & Grey, C. P. Identifying the local structures formed during lithiation of the conversion material, iron fluoride, in a Li ion battery: A solid-state NMR, X-ray diffraction, and pair distribution function analysis study. *Journal of the American Chemical Society* **131**, 10525–10536 (2009).

21. Doe, R. E., Persson, K. A., Meng, Y. S. & Ceder, G. First-principles investigation of the Li-Fe-F phase diagram and equilibrium and nonequilibrium conversion reactions of iron fluorides with lithium. *Chemistry of Materials* **20**, 5274–5283 (2008).

22. Murray, C. B., Kagan, C. R. & Bawendi, M. G. Synthesis and Characterization of Monodisperse Nanocrystals And Close-Packed Nanocrystal Assemblies. *International Journal of Advances in Engineering & Technology* **2**, 668–676 (2012).

23. Cargnello, M., Doan-Nguyen, V. V. T. & Murray, C. B. Engineering uniform nanocrystals: Mechanism of formation and self-assembly into bimetallic nanocrystal superlattices. *AIChE Journal* **62**, 392–398 (2016).

24. Huang, Q. *et al.* Insights into the Effects of Electrolyte Composition on the Performance and Stability of FeF2 Conversion-Type Cathodes. *Advanced Energy Materials* **9**, 1–11 (2019).

25. Gu, W., Magasinski, A., Zdyrko, B. & Yushin, G. Metal fluorides nanoconfined in carbon nanopores as reversible high capacity cathodes for Li and Li-ion rechargeable batteries: FeF2 as an example. *Advanced Energy Materials* **5**, 1–7 (2015).

26. Gordon, D. *et al.* Mixed Metal Difluorides as High Capacity Conversion-Type Cathodes: Impact of Composition on Stability and Performance. *Advanced Energy Materials* **8**, 1–10 (2018).

13

27. Chun, J. *et al.* Ammonium Fluoride Mediated Synthesis of Anhydrous Metal Fluoride-Mesoporous Carbon Nanocomposites for High-Performance Lithium Ion Battery Cathodes. *ACS Applied Materials and Interfaces* **8**, 35180–35190 (2016).

28. Song, H., Cui, H. & Wang, C. Extremely high-rate capacity and stable cycling of a highly ordered nanostructured carbon-FeF2 battery cathode. *J. Mater. Chem. A* **3**, 22377–22384 (2015).

29. Reddy, M. A. *et al.* CFx derived carbon-FeF2 nanocomposites for reversible lithium storage. *Advanced Energy Materials* **3**, 308–313 (2013).

30. Roth, H. G., Romero, N. A. & Nicewicz, D. A. Experimental and Calculated Electrochemical Potentials of Common Organic Molecules for Applications to Single-Electron Redox Chemistry. *Synlett* **27**, 714–723 (2016).

31. Pereira, N., Badway, F., Wartelsky, M., Gunn, S. & Amatucci, G. G. Iron Oxyfluorides as High Capacity Cathode Materials for Lithium Batteries. *Journal of The Electrochemical Society* **156**, A407 (2009).

32. Huang, Q. *et al.* Cycle stability of conversion-type iron fluoride lithium battery cathode at elevated temperatures in polymer electrolyte composites. *Nature Materials* (2019).

33. Tasaki, K. *et al.* Solubility of Lithium Salts Formed on the Lithium-Ion Battery Negative Electrode Surface in Organic Solvents. *Journal of The Electrochemical Society* **156**, A1019 (2009).

34. Tasaki, K. & Harris, S. J. Computational Study on the Solubility of Lithium Salts Formed on Lithium Ion Battery Negative Electrode in Organic Solvents Ken. *Journal of Physical Chemistry C* **114**, 8076–8083 (2010).

35. He, Z. & Alexandridis, P. Nanoparticles in ionic liquids: Interactions and organization. *Physical Chemistry Chemical Physics* **17**, 18238–18261 (2015).

36. Xie, Z.-h., Jiang, Z. & Zhang, X. Review — Promises and Challenges of In Situ Transmission Electron Microscopy Electrochemical Techniques in the Studies of. *Journal of The Electrochemical Society* **164**, 2110–2123 (2017).

37. Wang, C.-m. In situ transmission electron microscopy and spectroscopy studies of rechargeable batteries under dynamic operating conditions : A retrospective and perspective view. *Journal of Materials Research* **30**, 326–339 (2014).

38. Newman, J. & Thomas-Alyea, K. E. *Electrochemical Systems* (John Wiley & Sons, Inc., Hoboken, New Jersey, 2004), 3 edn.

39. Porter, D. A., Easterling, K. E. & Sherif, M. Y. *Phase Transformations in Metals and Alloys, Third Edition* (Taylor & Francis Group, Boca Raton, FL, 2009), 3 edn.

40. *CRC Handbook of Chemistry and Physics* (CRC Press, 2016).

41. Jain, A. *et al.* Commentary: The materials project: A materials genome approach to accelerating materials innovation (2013).

42. Cosandey, F., Al-Sharab, J. F., Badway, F., Amatucci, G. G. & Stadelmann, P. EELS spectroscopy of iron fluorides and FeFx/C nanocomposite electrodes used in Li-ion batteries. *Microscopy and Microanalysis* **13**, 87–95 (2007).

43. Dahmen, U. Orientation Relationships in Precipitation Systems. *Acta Metallurgica* **30**, 63–73 (1981).

Methods

Colloidal Synthesis of FeF$_2$ Nanorods. Trifluoroacetic acid (99%), trifluoroacetic anhydride (99%+), 1-octadecene (ODE, technical grade, 90%), and ethanol (absolute) were purchased from Fisher Scientific. Iron(II) chloride (98%), oleic acid (OLAC, technical grade, 90%), oleylamine (OLAM, technical grade, 90%), n-hexane (anhydrous, 95%), and chloroform (anhydrous, $\geq$ 99%) were purchased from Sigma-Aldrich. Ethanol was dried over calcium sulfate, filtered and stored over molecular sieves before use. All other chemicals were used as received.

Iron(II) trifluoroacetate, $Fe(CF_3COO^-)_2(CF_3COOH)_2$, was employed as the single source Fe, F precursor in the colloidal synthesis of FeF$_2$ nanorods. Iron(II) trifluoroacetate was prepared using a method modified from that developed by Guntlin *et al.*[44] Briefly, 3.5 g of iron(II) chloride and 40 ml of trifluoroacetic acid were loaded into a 50 ml Erlenmeyer flask, attached to a Schlenk line via a water-cooled condenser and heated to reflux on a hotplate under nitrogen flow with magnetic stirring for 24 h. Excess trifluoroacetic acid was evaporated under vacuum until a slushy, light brown mixture was obtained; the mixture was then washed three times with 10 ml portions of 5% trifluoroacetic anhydride in anhydrous hexane (v/v) followed by centrifugation. The resultant off-white, crystalline powder was dried under vacuum and transferred to an argon-filled glovebox.

In a typical FeF_2 nanorod synthesis, 1530 mg of the iron(II) trifluoroacetate (3 mmol) was transferred under argon to a 250 ml three-neck, round-bottom flask attached to a Schlenk line. To minimize air exposure, a continuous nitrogen purge was applied as 16 ml of oleic acid, 16 ml of oleylamine, and 28 ml of 1-octadecene were loaded into the flask along with a magnetic stir bar, resulting in a dark red solution. The flask was equipped with an immersion type thermocouple and a PID-controlled heating mantle and sealed with a ground-glass stopper. The reaction mixture was flushed under vacuum for (5 min) and purged under nitrogen (1 min) three times at room temperature and subsequently degassed under vacuum at 100 °C for 15 min. The flask was then heated to 310 °C ($\sim$14 °C/ min) resulting in a color change from dark red to clear yellow and allowed to react for 2 h. The reaction mixture was slowly cooled to room temperature, transferred to a centrifuge tube and washed 3 times by dispersion in anhydrous hexane followed by precipitation with dried ethanol and centrifugation. The washed pellet (260 mg) was redispersed and stored in anhydrous hexane resulting in a pale yellow dispersion.

Electrochemical Characterization. FeF_2 nanorod electrodes were fabricated using a conventional tape casting method. The as-synthesized FeF_2 nanorods were co-dispersed with a suspension of Super-P carbon black in anhydrous chloroform, dried under vacuum and hand ground with additional Super-P before mixing with polyvinylidene fluoride (PVDF) and N-methyl pyrrolidone (NMP). The resulting slurry (7:2:1 FeF_2:Super-P:PVDF by mass) was cast via doctor blade on aluminum foil, allowed to dry and placed under vacuum for 24 h before being punched into circular electrodes (diameter 1 cm). All electrodes tested contained between 1.0-1.3 mg cm^{-2}, corresponding to an areal capacity of 0.57-0.74 mA h cm^{-2} at a current density of 28.6-37.1 μA cm^{-2}.

Galvanostatic cycling tests were conducted at 30 °C between 4.0 and 1.2 V in a 2032 coin cell format using a Biologic BCS-805 battery cycler. Electrochemical impedance spectroscopy was performed in conjunction with galvanostatic cycling using 3-electrode Swagelok type cell and a Biologic VMP3 potentiostat. Impedance spectra in the frequency range 50 mHz – 200 kHz were acquired using a 10 mV amplitude, following a 1 h rest period after each discharge/charge half cycle (C/20 rate). All cells were assembled in an argon-filled glovebox using glass fiber separators (Whatman, GF/D) and metallic lithium foil (Sigma, 99.9%) as the counter/reference electrodes. The 1 molal IL electrolyte was prepared from LiFSI (TCI, >98%) and dried $Pyr_{1,3}FSI$ (Solvionic, 99.5%) in a glovebox. 1.0 M LP30 was purchased from Sigma-Aldrich.

Ex-situ XRD and XPS. Ex-situ samples from various states of discharge and charge were prepared by setting appropriate cutoff values for either voltage or charge during a galvanostatic cycling test at a C/20 rate. After a 2 h post-cycling rest, coin cells were transferred to an argon-filled glovebox and opened using a hydraulic disassembling press. The working electrodes were removed, patted dry and stored in dimethyl carbonate (DMC). For XRD measurements, electrodes were transferred in sealed vials to a Rigaku Miniflex XRD housed in a nitrogen-filled glovebox. XRD patterns were collected using a monochromated Cu K-α X-ray source from 10° to 60°, 2θ, at a scan rate of 1 °/ min. Contributions from the Al current collector were fitted using experimental data from pristine Al foil and subtracted. After measurement, the electrodes were returned to an Ar-filled glovebox and stored under DMC in preparation for ex-situ TEM measurements.

For XPS measurements, electrodes were soaked in DMC for 48 h and subsequently rinsed twice in fresh DMC to ensure removal of residual electrolyte. Electrodes were then transferred to a Schlenk tube under argon and dried under vacuum overnight. The electrodes were sealed under argon during transport and were only exposed to air for <1 min during transfer to the XPS high-vacuum chamber. XPS spectra were collected using a Thermo Scientific K-Alpha XPS with a monochromated Al K-α X-ray source. Data quantification was performed using Casa XPS software. All energy-loss regions in both survey and high-resolution spectra were fitted using Shirley-type backgrounds. A self-consistent peak model (Supplementary Figure 11) was developed for the pristine (uncycled) electrode and propagated to all other spectra with appropriate regions and components added to account for compounds introduced by the electrolyte. All spectra were charge referenced to the disordered C1s component at a binding energy of 284.8 eV.

Ex-Situ TEM/EDX/STEM/EELS. Following XRD measurements, the cycled electrodes were loaded into a glass vial with anhydrous NMP and a magnetic stir bar and gently stirred for 24 h under argon to remove and redisperse the electrode material. The dispersion was subsequently centrifuged at 14000 rpm for 10 min and the supernatant discarded. The resulting pellet was redispersed in fresh NMP, and drop cast on holey carbon TEM grids (Agar) in a glovebox on an 80 °C hot plate. Alternatively, to preserve the SEI, the electrodes in NMP were placed in an ultrasonic bath for 20 min and the resulting dispersion was immediately drop-cast onto TEM grids. All TEM samples were placed in a Schlenk tube under argon, dried under vacuum at 80 °C overnight, and transported to the TEM in airtight vials under argon. Air exposure

was limited to $<30\,$s during transfer to the TEM column.

Bright field TEM/HRTEM imaging was performed on a JEOL 3000F field emission gun transmission electron microscope operated at $300\,$kV and equipped with a Gatan Ultrascan CCD camera. EDX measurements were acquired in STEM mode with a $1\,$nm probe size using an Oxford instruments X-Max detector. Lattice reflections in the FFTs were measured based on their Gaussian centers of gravity and indexed by comparison with diffraction patterns computed from standard CIF files, using SingleCrystal software. FFTs were colored by changing the RGB values of only the white pixels in the original FFT using the "Selective Color" function in Adobe Photoshop to preserve the original appearance and relative intensity of diffraction spots. STEM/EELS measurements were conducted using a JEOL ARM 200F atomic resolution analytical microscope equipped with a Gatan GIF Quantum EELS detector. EELS spectra between 650 and $750\,$eV were collected at $200\,$kV with a $1\,$nm probe size and a dwell time of $0.5\,$s. Line scans were collected with a step size of $1.5\,$nm to minimize the accumulation of beam damage while maintaining acceptable spatial resolution. Spectra were calibrated to the zero-loss peak acquired simultaneously in dual-EELS mode. The backgrounds were subtracted using a power law model, and the Fe L_3/L_2 white line intensities were integrated after using a double arctangent function to fit the step background (Supplementary Figure 29). All image processing and EELS analysis was done using Gatan Microscopy Suite 3 software with plugins with the aid of additional scripts written by D. R. G. Mitchell.[45]

In-Situ TEM. In-situ lithiation experiments were performed using a Nanofactory Instruments Dual-Probe STM-TEM biasing sample holder within an FEI Tecnai G2 F20 X-Twin TEM at an accelerating voltage of $200\,$kV. The as-synthesized nanorods were dried, redispersed in acetonitrile and loaded onto a Cu wire probe via a simple dipping process. The Li metal counter electrode was prepared by attaching Li metal to a W wire and exposing it to air for $\sim5\,$s to generate a thin surface layer of Li_2O, functioning as a solid electrolyte. A relative bias of $-1.5\,$V was applied between the two electrodes to drive migration of Li^+ ions through the solid electrolyte. Video files were recorded through the live-view window in Gatan Digital Micrograph Software.

Data Availability

The authors declare that all data supporting the findings of this study are included within the paper and its supplementary information files. Source data is available from the corresponding authors upon reasonable request.

References

44. Guntlin, C. P., Kravchyk, K. V., Erni, R. & Kovalenko, M. V. Transition metal trifluoroacetates (M = Fe, Co, Mn) as precursors for uniform colloidal metal difluoride and phosphide nanoparticles. *Scientific Reports* **9**, 1–10 (2019).

45. Mitchell, D. R. G. DiffTools: Electron diffraction software tools for DigitalMicrograph$^{\text{TM}}$. *Microscopy Research and Technique* **71**, 588–593 (2008).

Acknowledgements

Author contributions

A.W.X. and M.P. conceived and designed the experiments. A.W.X. performed the experiments, analyzed the data and wrote the manuscript with inputs from all authors. H.J. assisted in the processing and Rietveld refinement of powder XRD data and provided helpful discussion regarding the interpretation of crystallographic data. I.C. assisted in the fabrication of electrodes, test cells and provided expertise regarding electrochemical testing. A.R. performed the collection of dark field STEM and EELS data. T.U.W and H.W.L. performed the in-situ TEM lithiation experiments and provided guidance on the interpretation in-situ data. J.F. prepared the ionic liquid electrolytes and provided advice on the properties of ionic liquids and the analysis of impedance data. S.W. assisted in

the collection of powder XRD patterns as well as editing and formatting of the manuscript. N.G. provided support for materials synthesis and experimental advice. M.P. supervised the design of the project, provided expertise on the interpretation of electrochemical data, and gave frequent, in-depth scientific input.

Competing Interests

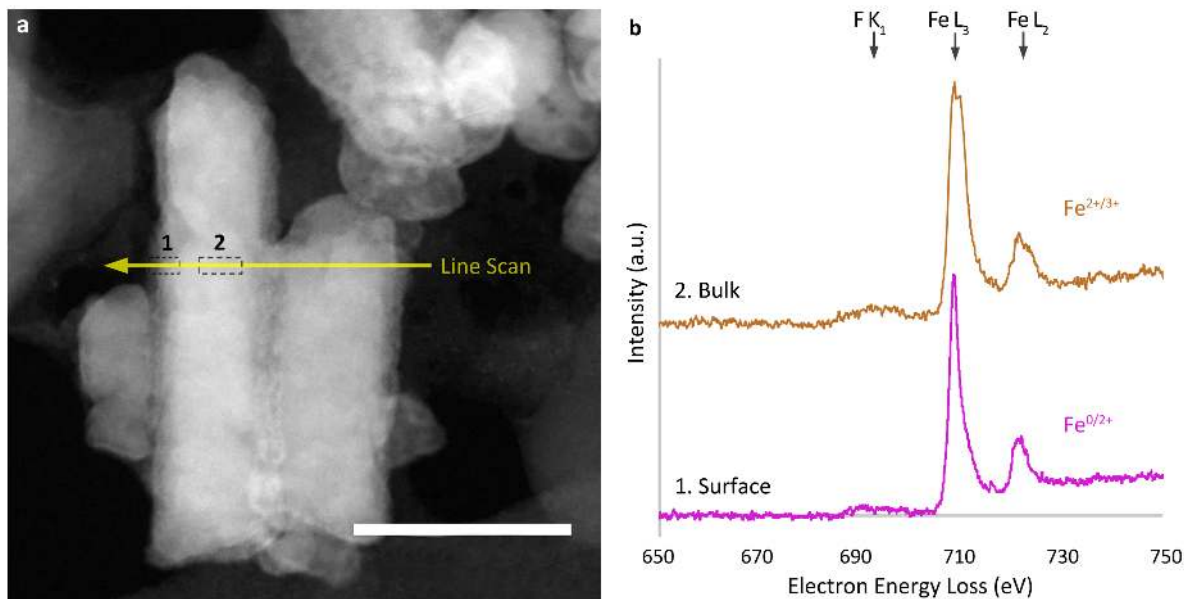The authors declare no competing interests.

Additional Information

Supplementary information is available for this paper

Extended data is available for this paper

Correspondence and requests for materials should be addressed to A.W.X or M.P.

**Reprints and permissions information** is available at www.nature.com/reprints.

Extended Data Fig. 1: Stage 2 (1.75 V, $x_{Li+} = 0.3$) **EELS Data. a,b,** Dark field STEM and corresponding EELS spectra for an FeF_2 nanorod from Stage 2 of discharge. Yellow arrows denote direction of EELS line scan and black dashed boxes indicate areas over which the displayed spectra are averaged. EELS spectra from the core of the nanrod exhibit a splitting of the Fe L_3 peak, specifically broadening toward higher energy loss values indicative of Fe^{3+}. The greater width of this peak is evident when compared to the EELS spectra acquired from the surface. This increase in Fe oxidation state indicates that a disproportionation to form the trirutile phase has occurred. This oxidation is not a result of air exposure as this would oxidize material at the surface first. Instead, the EELS spectra near the nanorod surface are still indicative of Fe^0 or Fe^{2+}. Scale bar, 40 nm (**a**).
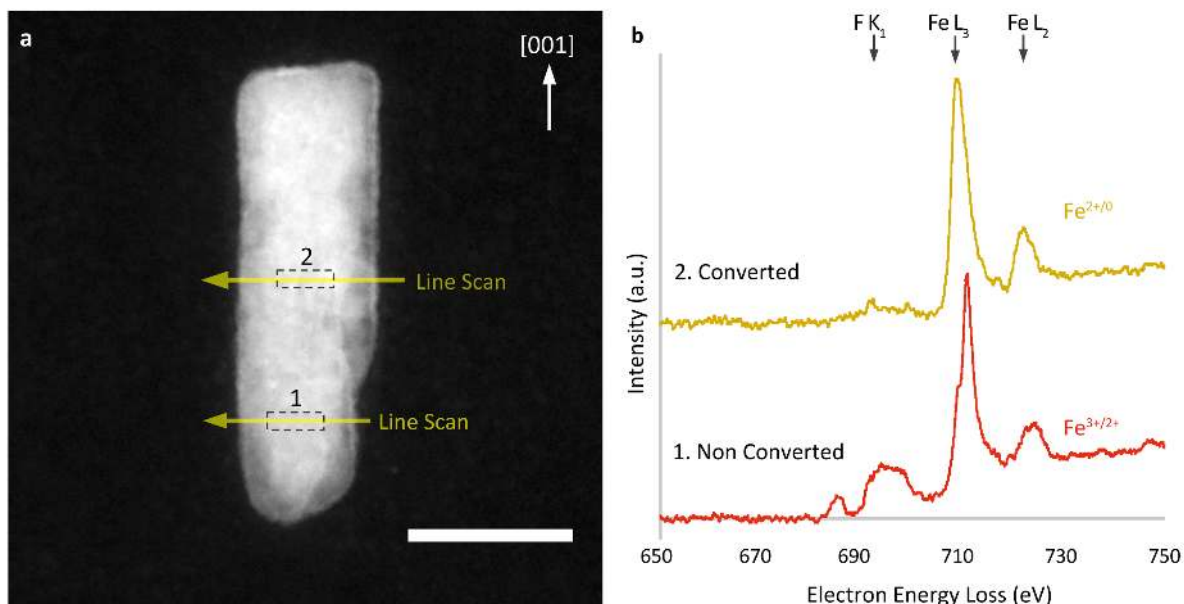
Extended Data Fig. 2: Stage 3 (1.7 V, $x_{Li+} = 1.0$) **EELS Data. a,b,** Dark field STEM and corresponding EELS spectra for an FeF_2 nanorod from Stage 3 of discharge. Line scans taken at different positions along the length of the nanorod indicate the presence of two distinct regions. There is a clear distinction between a region containing a strong Fe^{3+} signal related to the trirutile phase and a region containing only Fe^0 and Fe^{2+} species. This data suggests that the onset of conversion coincides with the reduction of the Fe^{3+} rutile formed during the initial disproportionation as well as the formation of metallic iron in the nanorod interior. Scale bar, 50 nm (**a**).
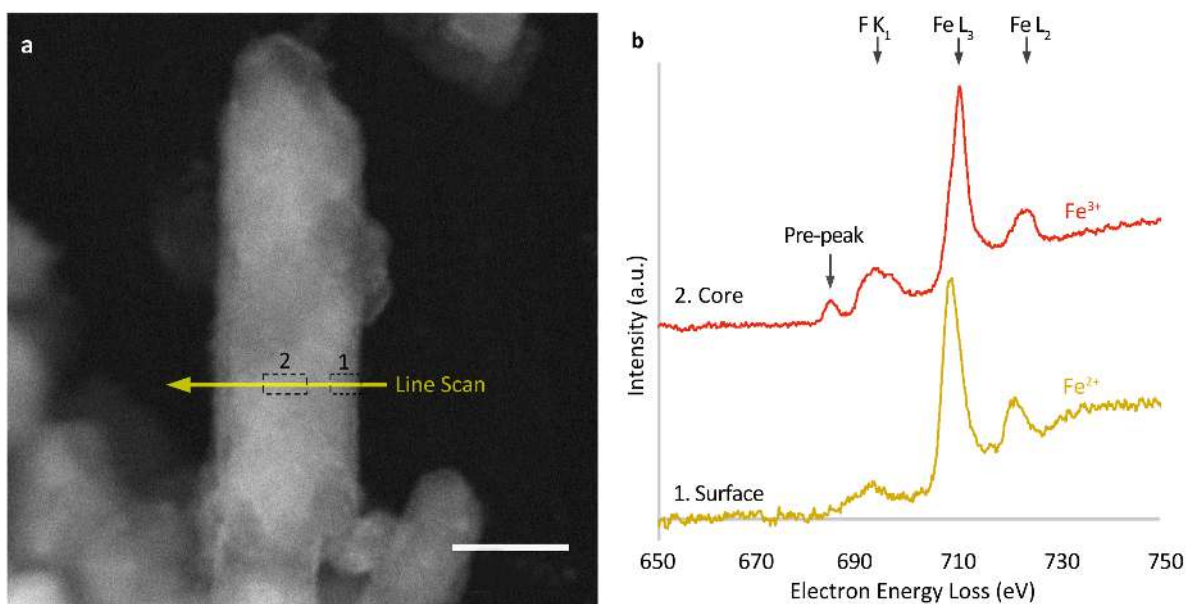
Extended Data Fig. 3: Stage 7 $(4.0\,\text{V}, x_{Li+} = 0.0)$ **EELS Data. a,b,** Dark field STEM and corresponding EELS spectra for an FeF_2 nanorod from Stage 3 of discharge. Upon charging to the full capacity at $4.0\,\text{V}$ vs. Li^+/Li, the widespread presence of Fe^{3+} is observed at the interior of the nanorod. This potential is higher than the standard reduction potential of $Fe^{3+} + e^- \rightarrow Fe^{2+}$ ($3.8\,\text{V}$ vs. Li^+/Li), and this transition is facilitated by the kinetically limited reinsertion of Fe from the double layer shell which causes the core of the nanorod to reconvert with a stoichiometry closer to FeF_3.[40] This delayed reconversion of the double layer shell is evidenced by EELS spectra from the nanorod surface, which show the distinct presence of Fe^{2+}. Fe^{3+} is generated at the beginning of discharge and reformed at the end of charge. Scale bar, 30 nm (**a**)
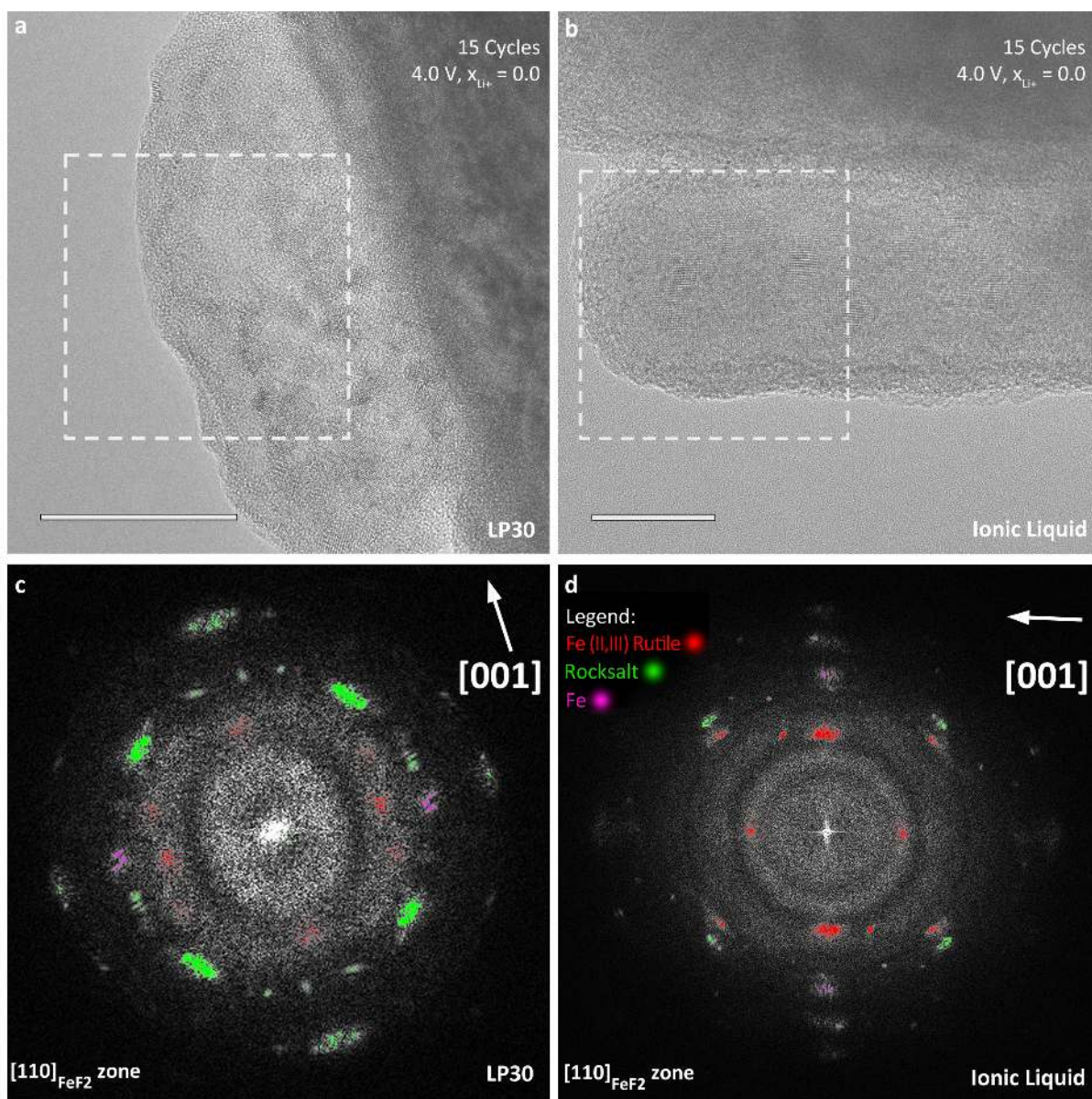
Extended Data Fig. 4: Nanorod structure after 15 cycles. a,b, Bright field TEM images comparing single nanorods after 15 cycles in the IL and LP30 electrolytes. **c,d,** The corresponding FFTs colored to differentiate between multiple phases present. Greater shape preservation is observed in the IL electrolyte. Strong rocksalt reflections in (**c**) indicate largely incomplete reconversion. Scale bars, 20 nm.